Available online at www.sciencedirect.com
ScienceDirect
Journal of the European Ceramic Society 28 (2008) 2301–2308
www.elsevier.com/locate/jeurceramsoc

Microstructures, crystallography of interfaces, and creep behavior of melt-growth composites

L. Mazerolles [a,*], L. Perriere [a,b], S. Lartigue-Korinek [a], N. Piquet [a,b], M. Parlier [b]

[a] *CECM, UPR 2801, CNRS, 15 rue Georges Urbain, F-94407 Vitry sur Seine, France*
[b] *ONERA/DMSC, 29 avenue de la Division Leclerc, F-92322 Châtillon Cedex, France*

Available online 4 March 2008

Abstract

Oxide eutectic ceramics were prepared from Al_2O_3 and Ln_2O_3-based systems by unidirectional solidification from the melt. The microstructure consists of two single-crystal phases continuously entangled in a three-dimensional interpenetrating network without grain boundaries, pores or colonies. The outstanding stability of these microstructures gives rise to a high strength and creep resistance at high temperature. Preferred growth directions, orientation relationships between phases and single-crystal homogeneity of specimens were revealed. Creep behavior at high temperature has been studied, mechanisms of deformation by dislocation motion and twinning were revealed from Transmission Electron Microscopy (TEM) observations. Extension to ternary eutectics with a three-dimensional microstructure consisting in the addition of a toughening phase (ZrO_2) to the previous binary eutectics has been investigated. By using this method, significant improvement of fracture toughness was obtained.

Keywords: Oxides; Ceramic eutectics; Microstructure; Creep; Dislocations

1. Introduction

In the field of structural materials, eutectic ceramic oxides prepared by solidification from the melt appear as potential candidates in the future for thermomechanical applications at very high temperature. Indeed, challenges related to future energy requirements impose the need to develop novel ultra-high-temperature structural materials which display good mechanical properties (tensile strength, creep resistance, fracture toughness) at temperatures above 1500 °C. For example in aircraft engines, the use of Ni-based single-crystal cast superalloys for turbine blades is only possible at temperatures lower than 1100–1150 °C. Silicon carbide-based composites are not stable enough in an oxidizing atmosphere when temperature is higher than 1300 °C and, finally, ceramic oxides, usually prepared by sintering, have a too high brittleness due to the grain boundaries and the amorphous phases observed at grain boundaries. Early studies on some oxide–oxide systems (such as Al_2O_3–ZrO_2) demonstrate the outstanding mechanical properties and the thermal and microstructural stability of directionally solidified eutectic ceramic oxides up to temperatures close to their melting point, as compared with conventional composites and monolithic ceramics.[1,2] Furthermore, oxide-based materials are very attractive because of their inherent thermochemical stability in oxidizing environments at high temperature. More recently, Waku et al. have developed binary eutectics, called melt-growth composites (MGC), with novel microstructures in which continuous networks of single-crystal Al_2O_3 phases and single-crystal oxide compounds interpenetrate without grain boundaries. These composites present a flexural strength constant from room temperature up to high temperatures and a good creep resistance allowing to consider applications in gas turbine and power generation systems with non-cooled turbine blades at very high temperatures.[3–5] In this paper, we will present results concerning similar microstructures obtained by directional solidification in various Al_2O_3 and Ln_2O_3-based systems. Morphology of microstructures, crystallography of constituent phases and interfaces, and single-crystal homogeneity of grown samples will be reported. Creep behavior at high temperature has been studied. Factors controlling the deformation mechanisms will be analyzed taking into account microstructural characteristics and Transmission Electron Microscopy (TEM) observations performed on deformed specimen. Finally, first results relative to the extension to ternary systems that display a significant increase of fracture toughness will be presented.

* Corresponding author.
E-mail address: mazerolles@glvt-cnrs.fr (L. Mazerolles).

0955-2219/$ – see front matter © 2008 Elsevier Ltd. All rights reserved.
doi:10.1016/j.jeurceramsoc.2008.01.014

Table 1
Chemical compositions and constituent phases of studied eutectics

Composition (mol%)	Eutectic phases	Structure of phases
$77Al_2O_3$–$23Gd_2O_3$	Al_2O_3–$GdAlO_3$	Corundum (hexagonal)
$76Al_2O_3$–$24Eu_2O_3$	Al_2O_3–$EuAlO_3$	+Perovskite (orthorhombic)
$81Al_2O_3$–$19Er_2O_3$	Al_2O_3–$Yb_3Al_5AlO_{12}$	Corundum (hexagonal)
$77Al_2O_3$–$23Y_2O_3$	Al_2O_3–$Y_3Al_5AlO_{12}$	+Garnet (cubic)

2. Experimental procedures

Fabrication from the melt of homogeneous eutectic microstructures requires planar growth front conditions in order to keep flat solid–liquid interfaces during growth at the macroscopic and microscopic level. These process conditions are obtained with equipments displaying high-thermal gradients in the solidification direction. Our experiments were carried out with a floating-zone translation device consisting in an arc image furnace operating with a 6-kW xenon lamp as a radiation source. Solidification was driven in air at a constant speed ranging from 2 to 20 mm h^{-1}. Cylindrical specimens of about 8 mm in diameter, and 50 mm in length were grown by this method. High-purity powders (99.99%) were used for starting materials. Before melting, these powders were mixed and molded in green cylinder bars by cold isostatic pressure then, consolidated by sintering at 1300 °C for 12 h.

Microstructural observations and chemical analyses of eutectic phases were performed by Scanning Electron Microscopy using a Leo 1530 (Leo, Germany) equipped with a Princeton Gamma Tech (USA) EDX spectrometer. They were carried out on sections of rods parallel and perpendicular to the growth direction. The crystalline homogeneity of specimen was controlled at the macroscopic scale (1–2 mm^2) by using the Electron Back Scattering Diffraction (EBSD) technique on a Zeiss DSM 950 microscope equipped with a TSL detector. Maps of the crystallographic orientations were obtained by this method. Growth directions, orientation relationships between eutectic phases and structure of interfaces were investigated by Transmission Electron Microscopy. These observations were performed on thinned foils of transverse sections using either a conventional microscope (JEOL 2000EX) or a high-resolution electron microscope (Topcon 002B) both operating at 200 kV.

From cylinder bars, compressive creep specimens were machined with dimensions of 3 mm × 3 mm × 5.5 mm, their major axis being parallel to the solidification direction. Constant-load compressive creep tests were conducted in air environment at 1450 and 1600 °C within the stress range from 70 to 200 MPa. Compression rams were made from sintered alumina with sapphire rods for applying loads on the specimen.

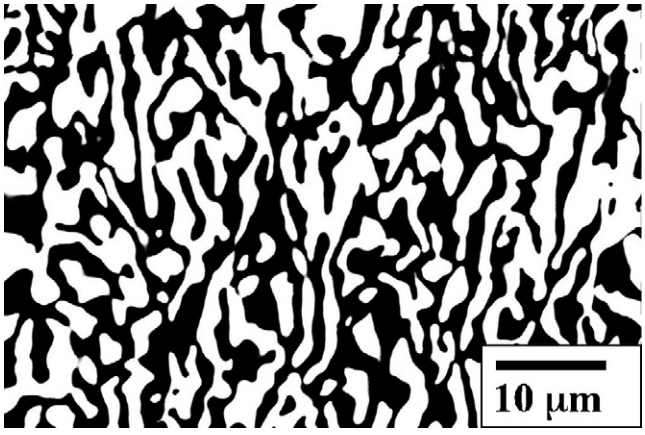

Fig. 2. Al_2O_3–Eu_2O_3 eutectic: SEM micrograph of longitudinal section.

3. Results and discussion

3.1. Microstructure

The studied eutectic composites were prepared in Al_2O_3–Ln_2O_3 systems. Phase diagrams of these systems all display an eutectic composition on the rich alumina side at temperatures close to 1800 °C. Eutectic phases consist in an α-Al_2O_3 phase (corundum structure) associated to either a perovskite-type phase $LnAlO_3$ (Ln = Sm, Eu, and Gd) or a garnet-type phase $Ln_3Al_5O_{12}$ for other elements of the lanthanides series. Data about the studied eutectic compositions are reported in Table 1.

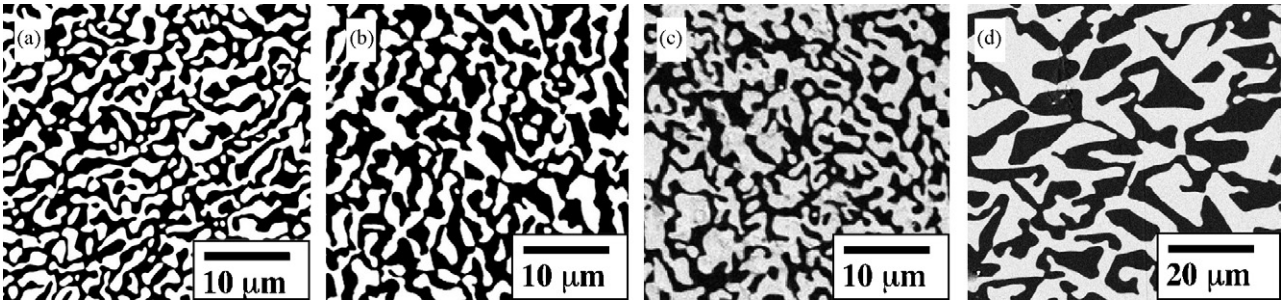

Fig. 1. SEM micrographs of directionally solidified eutectic cross-sections showing the interlocking microstructure ((a) Al_2O_3–Gd_2O_3; (b) Al_2O_3–Eu_2O_3; (c) Al_2O_3–Er_2O_3; (d) Al_2O_3–Y_2O_3). The white regions are perovskite (a and b) or garnet (c and d) and the black regions are alumina.

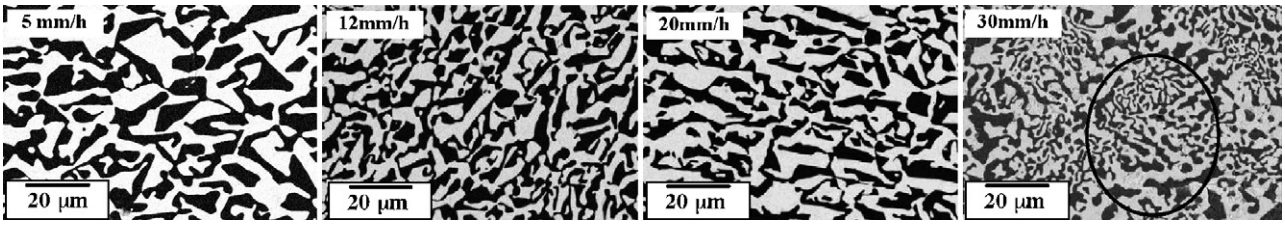

Fig. 3. Al_2O_3–Y_2O_3 eutectic: Morphology of microstructure *vs.* the solidification rate.

The eutectic microstructures grown in various composites are shown in Fig. 1. These SEM micrographs of sections perpendicular to the growth direction, reveal, in every case, continuous networks of an alumina phase (dark contrast) and lanthanide and aluminum oxide compounds ((a) GAP = $GdAlO_3$; (b) EAP = $EuAlO_3$; (c) EAG = $Er_3Al_5O_{12}$; (d) YAG = $Y_3Al_5O_{12}$). The observations performed on sections parallel (Fig. 2) to the growth direction show similar morphologies indicating the three-dimensional configuration of the microstructure. The two phases are continuously entangled in a three-dimensional interpenetrating network without grain boundaries, pores or colonies. The average size of each phase does not vary with the added rare-earth oxide except for the Al_2O_3–YAG composite (Fig. 1d). Indeed, at this eutectic composition, prepared at a growth rate (5 mm h^{-1}) similar to other composites, a microstructure with sharp angle facets and dimensions about five times larger than that of other eutectics has been observed. This difference could be related to the diffusion coefficient values of yttrium higher than that of lanthanide elements. However, for the Al_2O_3–YAG eutectic, a microstructure displaying dimensions very similar to other Al_2O_3–Ln_2O_3 eutectics without modifying the Chinese script morphology has been produced for growth conditions with much higher solidification rates.[6]

In most directionally solidified oxide eutectics, coupled growth is mainly controlled by the growth rate. For example, in the case of the Al_2O_3–$ZrO_2(Y_2O_3)$ eutectic, the planar growth regime, leading to zirconia fibers embedded in an alumina matrix, only exists at very low solidification rates (<5 mm h^{-1} by using an arc image furnace). When this rate increases the eutectic growth undergoes a transition from the planar to the cellular regime that does not correspond anymore to a coupled growth.[7] Fig. 3 reveals that the three-dimensional microstructure of the Al_2O_3–YAG eutectic, is not immediately modified when the growth rate increases and persists up to rates close to 30 mm h^{-1} with similar solidification conditions (thermal gradient, diameter of specimen) before entering into the cellular growth regime (Fig. 3). Similar results were obtained with the other eutectic compositions.

3.2. Crystallography and interfaces

Aligned eutectic microstructures (lamellae, fibers or dispersoids), grown by unidirectional solidification, usually consist of single-crystal phases growing preferentially along well-defined crystallographic directions. These directions are not necessarily the directions of easy-growth of the components but often correspond to minimum interfacial energy configurations between phases. These perfectly aligned lattices are related by orientation relationships which are unique in most systems and produce well-defined interface planes corresponding to dense atomic arrangements in the component phases.[8–11] Contrarily to these aligned microstructures, interconnected microstructures, shown in the previous figures, display a very isotropic morphology. However, electron diffraction studies performed on thin plates cut perpendicularly to the rod axes reveal growth directions also corresponding to well-defined crystallographic directions.

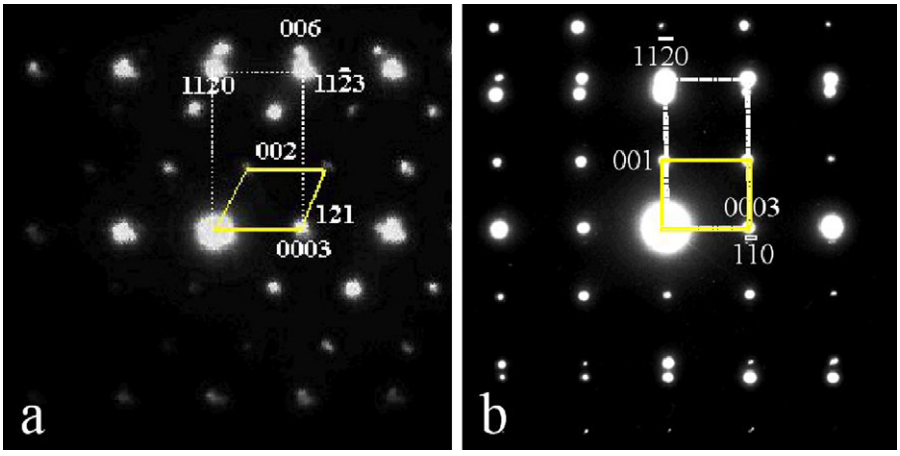

Fig. 4. Electron diffraction patterns performed at the Al_2O_3–YAG (a) and Al_2O_3–$EuAlO_3$ (b) interfaces.

Table 2
Growth directions and orientation relationships of eutectic phases in the Al_2O_3–Ln_2O_3 eutectics

Eutectic phases	Growth directions	Orientation relationships
Al_2O_3–$LnAlO_3$ (Ln = Gd, Eu)	$[1\,0\,\bar{1}\,0]Al_2O_3$//[1 1 0]perovskite or $[1\,1\,\bar{2}\,0]Al_2O_3$//[0 0 1]perovskite	$(1\,1\,\bar{2}\,0)\,Al_2O_3$//(0 0 1) perovskite (0 0 0 1) Al_2O_3//(1 0 0) perovskite
Al_2O_3–$Ln_3Al_5O_{12}$ (Ln = Er, Dy, Yb, Y))	$[1\,0\,\bar{1}\,0]Al_2O_3$ $\langle 2\,\bar{1}\,0\rangle$ or $\langle 1\,1\,0\rangle$ garnet	$(0\,0\,0\,1)Al_2O_3$//(1 2 1)garnet

In these eutectic composites, the most frequently observed growth direction for Al_2O_3 was $[1\,0\,\bar{1}\,0]$. Sometimes, the $[1\,1\,\bar{2}\,0]$ direction was also observed but, in all cases, the basal plane of the corundum structure is always parallel to the solidification axis whatever the considered eutectic system. The electron diffraction patterns shown in Fig. 4 were performed on platelets cut perpendicularly to the growth directions of Al_2O_3–YAG and Al_2O_3–GAP eutectics. The selected area aperture is centered on the interface, and consequently diffraction spots of both phases are superimposed on the same pattern. Crystallographic principal directions are strictly aligned according to the following relations:

$$(0\,0\,0\,1)Al_2O_3//(1\,2\,1)Y_3Al_5O_{12}$$

$$\text{and :}\quad (1\,1\,\bar{2}\,0)Al_2O_3//(0\,0\,1)GdAlO_3$$

Other growth directions of the garnet phase were also observed ($\langle 1\,1\,0\rangle$ in major cases) but the orientation relationship between the two phases persisted. In the case of eutectics associating perovskite and corundum structures, two sets of orientation relations were determined. These results are summarized in Table 2.

EBSD studies have shown that these preferred growth directions and orientation relationships are retained on a large central part of the specimen[12] and confirmed the single-crystal quality of grown samples.

The minimal energy configuration at the interfaces is well illustrated by the HRTEM image (Fig. 5a) of the interface between the corundum and perovskite structures for the Al_2O_3–$EuAlO_3$ eutectic. This image corresponds to a eutectic structure grown along the $[1\,1\,\bar{2}\,0]$ alumina and [0 0 1] perovskite directions. No intermediary phase is detected at the interface and the transition on both sides of the interface operates on one or two atomic planes. Bragg filtering in the reciprocal space, from the numerical Fourier Transform of the digitized image, reveals that accommodation between the two structures is restored by a periodic array of dislocations along the interface (Fig. 5b). Similar results were also obtained with eutectics consisting of garnet and alumina phases. These TEM observations did not reveal any stress fields at the interfaces, and are in good agreement with low values of residual stresses measured at room temperature from X-ray diffraction experiments[13] or from spectroscopic studies through the shift of fluorescence lines of Cr in sapphire.[14]

3.3. Compressive creep deformation

Fig. 6 shows a typical strain *vs.* time relationship for the Al_2O_3–YAG eutectic in a compressive test at 1450 °C with stresses ranging from 70 to 200 MPa. The creep deformation curves show a primary creep regime where the deformation rate decreases continuously. After this short primary stage (e.g. strain of about 0.5%), when the secondary creep rate is reached, the applied load is modified and primary and secondary creep rates

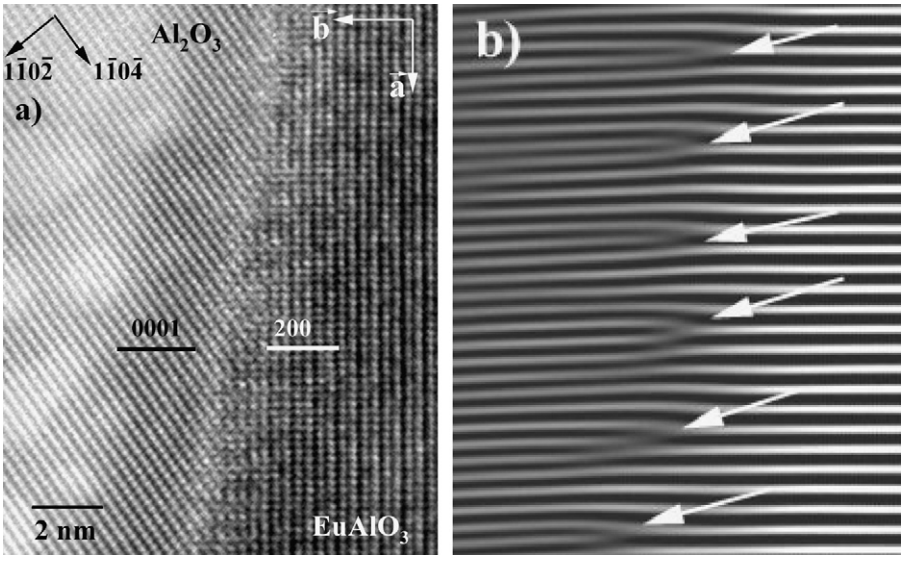

Fig. 5. (a) HRTEM image of the Al_2O_3–$EuAlO_3$ interface. (b) Inverse Fourier Transform from the digitized image of the (a) interface built with $0\,0\,0\,3_{Al_2O_3}$ and $2\,0\,0_{EuAlO_3}$ Bragg spots.

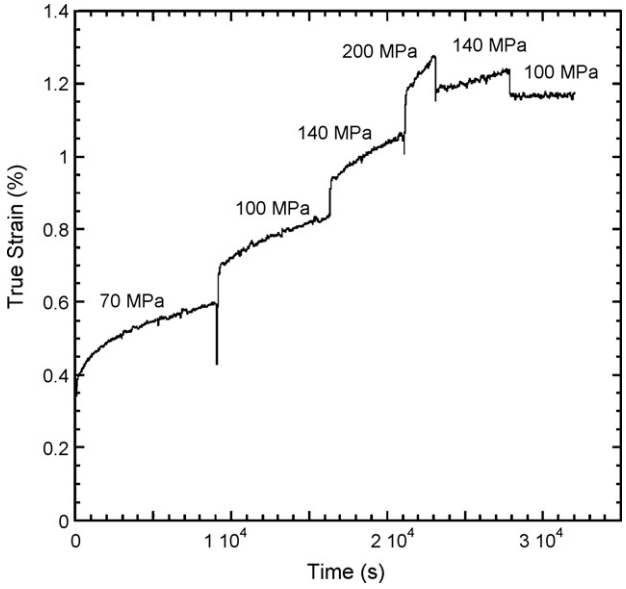

Fig. 6. Al_2O_3–YAG eutectic: Creep curve at 1450 °C with load increments and decrements (70, 100, 140, 200 then 140 and 100 MPa).

are again measured at a higher stress. The secondary creep rate $\dot{\varepsilon}$ is very sensitive to the applied stress σ following a power–law relationship:

$$\dot{\varepsilon} = A\sigma^n \exp\left(-\frac{Q}{RT}\right)$$

where A is a material constant, n is the stress exponent, Q is the activation energy for creep, R is the gas constant and T is the absolute temperature. The quasi-steady-state regime in this work was determined by plots of the strain rate as a function of the true strain (Fig. 7). Fig. 8 shows the quasi-steady-state rates for the eutectics and regime stress tested. These plots reveal the high creep resistance of these interlocked microstructures with strain rates very similar to that of Al_2O_3–ZrO_2 eutectics[15,16] at

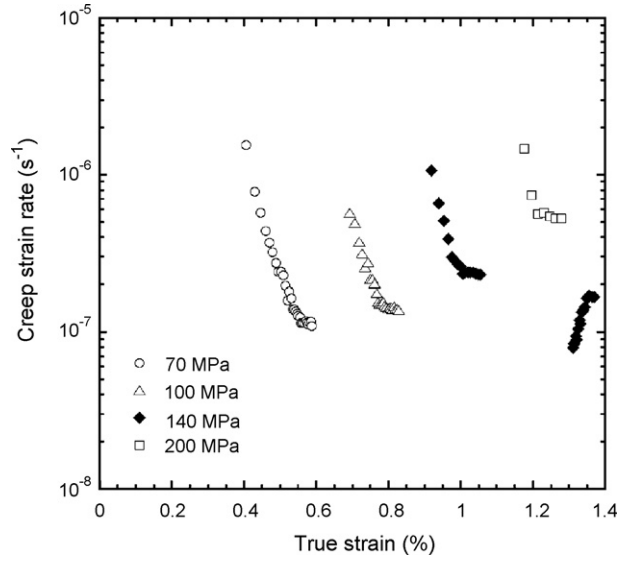

Fig. 7. Strain rates as a function of true strain allowing to determine the minimum creep rates corresponding to the quasi-steady-state regime in various eutectics.

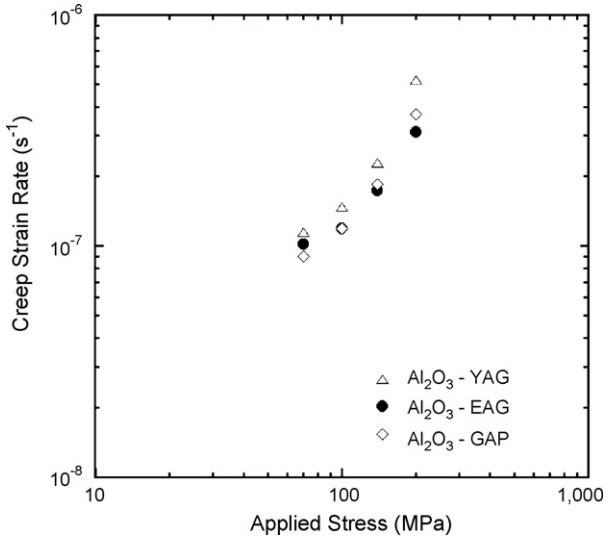

Fig. 8. Plot of the creep rates *vs.* the applied stress for various eutectics.

low stresses (<140 MPa) and even higher at high stresses. This behavior is especially noteworthy as the Al_2O_3–ZrO_2 eutectic has melting temperature (T_m = 1910 °C) higher than that of Al_2O_3–Ln_2O_3 eutectics (1710 < T_m < 1827 °C). Consequently, for the same T/T_m, these former display a better creep resistance.

The incremental application of the load during one single experiment allows to determine readily the n exponent at each stress step by extrapolation of the minimum creep rate values for a given strain value. Eventual changes of the n value for various applied stresses reveal different creep mechanisms. From the results summarized in Table 3 we can see that the n value is higher than 2 from a 100–140 MPa step suggesting a deformation mechanism controlled by a dislocation motion. Values close to 4 have also been measured for creep tests performed at 1600 °C. These high stress components are incompatible with the interpretation of plasticity controlled by pure diffusion. In the case of deformation due to pure lattice diffusion or grain boundary diffusion the resulting creep rate is linearly proportional to the stress and $n = 1$.[17] Moreover, HRTEM images of interfaces (Fig. 5) indicate a considerable coherence and strong bonding between phases at the interfaces and consequently boundary sliding mechanisms are impossible. TEM studies were performed on these specimens deformed at 1600 °C. Images presented in Fig. 9 corresponding to the Al_2O_3–GAP eutectic, clearly show dislocations in the two eutectic phases.

In alumina, the dislocations observed in Fig. 9a are basal-type dislocations ($b = 1/3[2\,\bar{1}\,\bar{1}\,0]$) aligned in parallel basal slip planes (0 0 0 1). The basal plane is seen edge-on in this orientation. The basal slip system has the lowest critical resolved shear

Table 3
Values of the stress exponent as a function of the stress increment for various Al_2O_3–Ln_2O_3 eutectics deformed at 1450 °C

	70 → 100 MPa	100 → 140 MPa	140 → 200 MPa
Al_2O_3–GAP	1.10	2.08	2.60
Al_2O_3–EAG	1.20	2.10	2.72
Al_2O_3–YAG	1.13	2.06	2.99

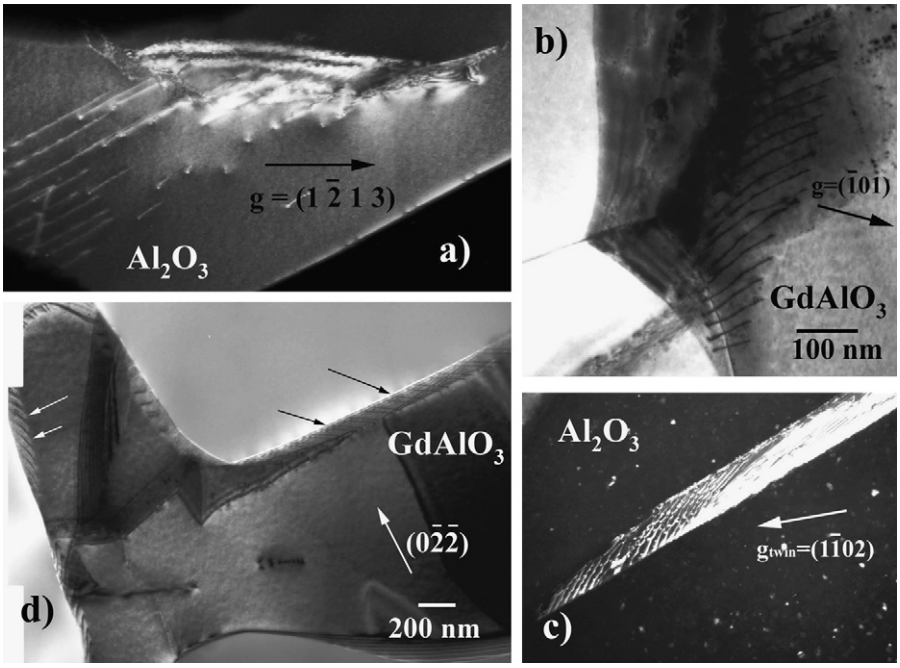

Fig. 9. TEM images of microstructural features in Al_2O_3–GAP sample after compressive deformation at 1600 °C. (a) 2-Beam dark field image showing dislocations in basal planes in the alumina phase. (b) Bright field image showing a dislocation pile-up into the GAP phase and a basal twin occuring in alumina at the interaction between the pile-up and the interface. (c) Dark field image (with a twin diffraction vector) revealing dislocations in the twin boundaries. (d) Bright field image: Two isolated dislocations occur inside the GAP phase. Interfaces display dislocations arranged by pairs (indicated by arrows).

stress at high temperature.[18] Fig. 9b shows a dislocation pile-up in the GAP phase. The pile-up interacts with the GAP–alumina interface at the bottom of the image, and a basal twin is seen in alumina close to the interaction. The twin has probably occurred by accommodation of stresses resulting from the pile-up. Dislocations are present in the twin boundaries (Fig. 9c). It is worth noting that usually large stresses are necessary to activate basal twins. Only in a few cases, basal twinning has been observed in alumina submitted to plastic deformation.[19,20] These observations are in agreement with the high value of the stress component.

Finally, interfacial dislocations arranged by pairs are present in most interfaces (Fig. 9d). Work is underway to understand the origin of these defects, either from misfit dislocations or resulting from the interaction with lattice dislocations.

We can note from results presented in Table 3 when the stress is higher than 140 MPa, that the n value corresponding to the Al_2O_3–YAG eutectic is slightly higher than that of the two other eutectics indicating a higher creep rate. If we consider that the stress required to drive a dislocation across the interfaces is at least two orders of magnitude higher than the resolved stresses applied in the tests,[21] both phases must deform independently in order to creep at the same rate. Consequently, the dislocations have to move in each component and must bow within the phase spacing (λ). The stress necessary for this process is:

$$\tau = \frac{Gb}{\lambda}$$

where G is the shear modulus and b the Burgers vector.[22] Consequently, when the size of microstructure decreases (it is the case of Al_2O_3–EAG and Al_2O_3–GAP eutectics) the glide of dislocations require higher stresses to be activated.

3.4. Extension to ternary systems

Despite a high flexural strength reported in the literature, a good thermal stability and an outstanding creep resistance at high temperature as we have seen previously, the Al_2O_3–Ln_2O_3 eutectics (particularly for systems containing a garnet phase) display a low fracture toughness at room temperature. We tried to increase the K_{IC} values by the addition of a toughening phase (ZrO_2) to these binary eutectics without modifying the three-dimensional interpenetrating network. This singular microstructure observed in binary systems results from eutectic coupled-growth conditions. Consequently, we looked for preparing ternary eutectic compositions in the Al_2O_3–Ln_2O_3–ZrO_2 systems with the same growth conditions. The phase diagrams of these systems are not well known. One eutectic composition has been reported and prepared in the $Al_2O_3/ZrO_2/Y_2O_3$ system[23] but for other rare-earth oxides very few experimental data are available except phase diagrams calculated with CALPHAD methods.[24] We experimentally determined the eutectic composition $58Al_2O_3$–$19Gd_2O_3$–$23ZrO_2$ (mol%) from microstructural observations. Similarly to binary eutectics, the as prepared microstructures consist of an interpenetrated network of two major eutectic phases and the zirconia phase is located at the interfaces between the alumina and garnet (or perovskite) type phases. ZrO_2 is fully stabilized by the rare-earth ions in the fluorite structure (Fig. 10).

In the case of the Al_2O_3–Y_2O_3–ZrO_2 eutectic, the comparison with the binary eutectic, reveals a significant decrease of the

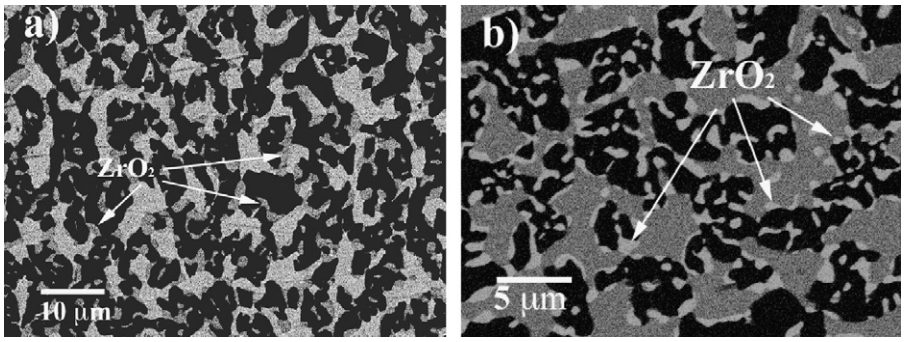

Fig. 10. SEM micrographs of ternary eutectics: (a) Al_2O_3–Y_2O_3–ZrO_2; (b) Al_2O_3–Gd_2O_3–ZrO_2. Alumina phase corresponds to dark contrast, YAG and GAP phases to the grey contrast and zirconia phase is indicated by arrows.

mean size of microstructure and changes of morphology (growth facets have disappeared) likely due to growth mechanisms modified by the third eutectic phase. The single-crystal homogeneity is not modified by the addition of a third phase. The electron diffraction studies revealed the following growth directions:

$[1\,0\,\bar{1}\,0]Al_2O_3//[0\,0\,1]Y_3Al_5O_{12}//[0\,0\,1]ZrO_2$

and the epitaxial relationships between constituent phases:

$(0\,0\,0\,1)Al_2O_3//(1\,0\,0)ZrO_2(0\,0\,0\,1)Al_2O_3//(0\,0\,1)Y_3Al_5O_{12}$

The same epitaxial relations between alumina and zirconia phases were already observed for the Al_2O_3–ZrO_2 binary eutectic[9] but the preferred growth direction of the garnet structure observed in the binary systems is modified by the addition of zirconia and occurs along the $\langle 1\,0\,0\rangle$ direction in the ternary system. Similarly to the results obtained on binary eutectics, the EBSD analysis confirmed the single-crystal homogeneity on large areas (some millimeters). The pole figures (density maps) relative to the Al_2O_3–Y_2O_3–ZrO_2 eutectic shown in Fig. 11, reveal single growth directions for the three constituent phases in the analyzed area (the highest density of the $1\,0\,\bar{1}\,0_{Al_2O_3}$, $0\,0\,1_{YAG}$ and $0\,0\,1_{ZrO_2}$ orientations is located in the center of the stereographic projections corresponding to the normal to the surface). Localization of poles on the great circle is also in agreement with electron diffraction results.

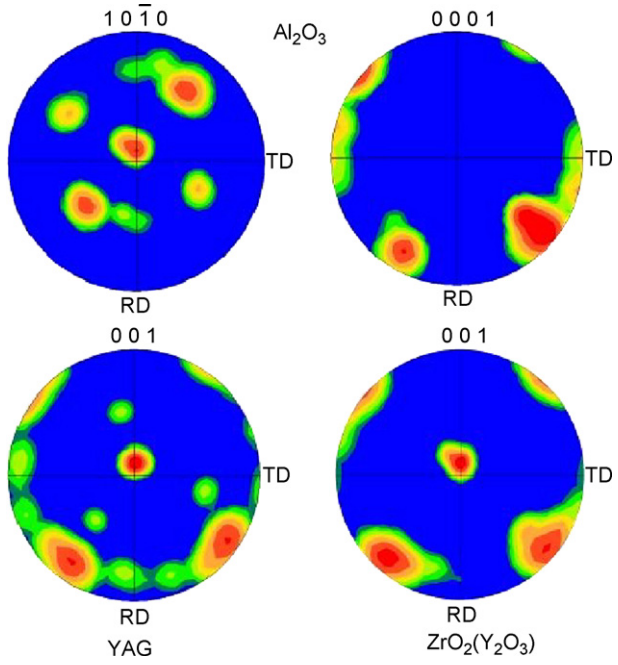

Fig. 11. Al_2O_3–YAG–ZrO_2 eutectic: EBSD pole figures of a 1.75 mm × 1.75 mm area corresponding to the $0\,0\,0\,1_{Al_2O_3}$, $1\,0\,\bar{1}\,0_{Al_2O_3}$, $0\,0\,1_{YAG}$ and $0\,0\,1_{ZrO_2}$ orientations.

The addition of ZrO_2 phase to the binary systems gives rise to a significant increase of fracture toughness. The most important effect was observed in the case of eutectics associating alumina and garnet phase. Mechanism of crack deflection by the zirconia phase coupled with the decrease of the size of microstructure resulted into an increasing of the K_{IC} values of about 70%.[25] This effect is less significant for the eutectics containing a perovskite phase but a systematic increase of about 15% was also measured.[12] Study of creep behavior of these ternary eutectics is in progress.

4. Conclusion

Our study on the oxide eutectic composites grown from the melt has shown that the outstanding mechanical properties at low or high temperature could result from the combination of different factors. Firstly, eutectic composition gives rise to a very good chemical and thermal stability of the microstructure up to temperatures close to the melting temperature. The very isotropic morphology of that microstructure in the Al_2O_3–Ln_2O_3 systems, induces a mechanical behavior that will not depend on the direction of the applied mechanical stress. Growth of these eutectics, whatever the rare-earth oxides associated to alumina and solidification conditions, follows a small set of crystallographic directions often corresponding to dense atomic rows of structures. These directions do not change all over the specimen, and consequently a very low amount of grain boundaries, often at the origin of brittleness phenomena, is observed. The absence of intermediary phase at the interfaces and the crystallographic orientation relationships between phases give rise to a strong cohesion between components. The outstanding creep resistance of these materials is likely related to the quality of these interfaces. TEM studies revealed deformation mechanisms by dislocation motion in the two phases with pile-up phenomena at the interfaces. Other mechanisms, such as basal twinning in alumina usually requiring large stresses, were also observed.

In order to increase fracture toughness of binary eutectics, a third phase (ZrO_2) was added. These composites were prepared at a ternary eutectic composition. A new eutectic composition was determined for the Al_2O_3–Gd_2O_3–ZrO_2 system and interconnected microstructures were successfully grown. The single-crystal homogeneity of composites was preserved with preferred growth directions and orientation relationships between phases. Fracture toughness was improved by a factor ranging from 1.5 to 1.7 compared to binary systems. Creep behavior of these ternary eutectics compared to the binary systems and the investigation of deformation mechanisms from TEM observations is in progress.

Acknowledgements

The authors would like to thank D. Boivin (ONERA/DMMP) for the EBSD studies. L. Perrière would also like to thank the French Defence Research Organization (DGA) for a Doctorate Studentship.

References

1. Hulse, C. O. and Batt, J. A. The effect of eutectic microstructures on the mechanical properties of ceramic oxides. Final. Rept UARL-N910803-10, NTIS AD-781995/6GA, 1974.
2. Minford, W. J., Bradt, R. C. and Stubican, V. S., Crystallography and microstructure of directionally solidified oxide eutectics. *J. Am. Ceram. Soc.*, 1979, **62**, 154–157.
3. Waku, Y., Nakagawa, N., Wakamoto, T., Ohtsubo, H., Shimizu, K. and Kohtoku, Y., A ductile ceramic eutectic composite with high strength at 1873 K. *Nature*, 1997, **389**, 49–52.
4. Ochiai, S., Ueda, T., Sato, K., Hojo, M., Waku, Y., Nakagawa, N. *et al.*, Deformation and fracture behavior of an Al_2O_3/YAG composite from room temperature to 2023. *Comp. Sci. Technol.*, 2001, **61**, 2117–2128.
5. Nakagawa, N., Ohtsubo, H., Mitani, A., Shimizu, K. and Waku, Y., High temperature strength and thermal stability for melt growth composite. *J. Eur. Ceram. Soc.*, 2005, **25**, 1251–1257.
6. Pastor, J. Y., Llorca, J., Salazar, A., Oliete, P. B., de Fransisco, I. and Pena, J. I., Mechanical properties of melt-grown alumina–yttrium aluminium garnet eutectics up to 1900 K. *J. Am. Ceram. Soc.*, 2005, **88**, 1488–1495.
7. Echigoya, J., Takabayashi, Y., Sasaki, K., Hayashi, S. and Suto, H. J., Solidification microstructure of Y_2O_3-added Al_2O_3–ZrO_2 eutectic. *Trans Jpn. Inst. Met.*, 1986, **27**, 102–107.
8. Stubican, V. S. and Bradt, R. C., Eutectic solidification in ceramic systems. *Ann. Rev. Mater. Sci.*, 1981, **11**, 267–297.
9. Mazerolles, L., Michel, D. and Portier, R., Interfaces in oriented Al_2O_3–$ZrO_2(Y_2O_3)$ eutectics. *J. Am. Ceram. Soc.*, 1986, **69**, 252–255.
10. Revcolevschi, A., Dalhenne, G. and Michel, D. External and internal interfaces of metal oxides. *Mater. Sci. Forum*, Trans. Tech. Publications, 1988, 173–197.
11. Mazerolles, L., Michel, D. and Hÿtch, M. J., Microstructure and interfaces in directionally solidified oxide–oxide eutectics. *J. Eur. Ceram. Soc*, 2005, **25**, 1389–1395.
12. Mazerolles, L., Piquet, N., Trichet, M. F. and Parlier, M., Microstructures and interfaces in melt growth Al_2O_3–Ln_2O_3 based eutectic composites. *Adv. Sci. Technol.*, 2006, **45**, 1377–1384.
13. Dickey, E. C., Frazer, C. S., Watkins, T. R. and Hubbard, C. R., Residual stresses in high temperature ceramic eutectics. *J. Eur. Ceram. Soc.*, 1999, **19**, 2503–2509.
14. Gouadec, G., Colomban, Ph., Piquet, N., Trichet, M. F. and Mazerolles, L., Raman/Cr^{3+} fluorescence mapping of a melt-grown Al_2O_3/$GdAlO_3$ eutectic. *J. Eur. Ceram. Soc.*, 2005, **25**, 1447–1453.
15. Argon, A. S., Yi, J. and Sayir, A., Creep resistance of directionally solidified eutectics of Al_2O_3/$cZrO_2$ with sub-microncolumnar morphologies. *Mater. Sci. Eng.*, 2001, **A319**, 838–842.
16. Yi, J., Argon, A. S. and Sayir, A., Creep resistance of the directionally solidified ceramic eutectic of Al_2O_3/$cZrO_2(Y_2O_3)$: experiments and models. *J. Eur. Ceram. Soc.*, 2005, **25**, 1201–1214.
17. Poirier, J., *Creep of Crystals*. Cambridge University Press, Cambridge, 1985.
18. Lagerloff, K. P. D., Heuer, A. H., Castaing, J., Rivière, J. P. and Mitchell, T. E., Slip and twinning in sapphire (α-Al_2O_3). *J. Am. Ceram. Soc.*, 1994, **77**, 385–397.
19. Heuer, A. H., Lagerlof, K. P. D. and Castaing, J., Slip and twinning dislocations in sapphire (α-Al_2O_3). *Phil. Mag. A*, 1998, **78**, 747–763.
20. Lartigue-Korinek, S. and Dupau, F., Grain boundary behavior in superplastic Mg-doped alumina with yttria codoping. *Acta Metall. Mater.*, 1994, **42**, 293–302.
21. Martinez Fernandez, J. and Sayir, A., Creep of directionally solidified Al_2O_3/$Er_3Al_5O_{12}$ fibers with hypo-eutectic composition. *Ceram Eng. Sci. Proc.*, 2001, **22**, 421–428.
22. Hirth, J. P. and Lothe, J., *Theory of Dislocations*. John Wiley & Sons, 1982.
23. Waku, Y., Sakata, S., Mitani, A. and Shimizu, K., Temperature dependence of flexural strength and microstructure of Al_2O_3–$Y_3Al_5O_{12}$–ZrO_2 ternary melt grown composites. *J. Mater. Sci.*, 2002, **37**, 2975–2982.
24. Lakiza, S. M., Fabrichnaya, O., Wang, Ch., Zinchevich, M. and Aldinger, F., Phase diagram of the ZrO_2–Al_2O_3–Gd_2O_3 system. *J. Eur. Ceram. Soc.*, 2006, **26**, 233–246.
25. Perriere, L., Valle, R., Mazerolles, L. and Parlier, M., Crack propagation in directionally solidified eutectic ceramics. *J. Eur. Ceram. Soc.*, 2008, **28**, 2337–2343.